RPE | Radiation Physics & Engineering
An International Peer-Reviewed Journal
Published by K.N. Toosi University of Technology
http://rpe.kntu.ac.ir
Research Article

Radiation Physics and Engineering 2022; 3(1):1–12
https://doi.org/10.22034/RPE.2021.318027.1046

Feasibility study on the use of SPECT for boron dose imaging in TRR-based BNCT

Mahdieh Sadat Mousavi, Faezeh Rahmani*
Department of Physics, K.N. Toosi University of Technology, P.O. Box 15875-4416, Tehran, Iran

HIGHLIGHTS

- The requirement for online monitoring boron dose in BNCT to ensure the effectiveness of the treatment.
- Optimization of an imaging system based on SPECT for online dosimetry in BNCT based on TRR.
- Reconstruction of B-10 concentration distribution map in tumor phantom by MLEM method.

ABSTRACT

Boron Neutron Capture Therapy (BNCT) is one of the promising treatment methods for some malignant tumors such as Glioblastoma Multiforme (GBM). One of the requirements of BNCT treatment is the accurate and real-time boron-concentration monitoring to ensure the efficacy of treatment and no leakage of boron. An accurate method for real-time calculation of the boron dose distribution mapping during irradiation is Single Photon Emission Computed Tomography (SPECT), in which the determination of boron distribution is based on the detection of 478 keV prompt gamma-rays generated through thermal neutron capturing by B-10. Tehran Research Reactor (TRR) is the only possible source for BNCT in Iran, so as the first approach, this BNCT-SPECT system has been evaluated for TRR. In this paper, an imaging system of BNCT-SPECT including four arrays of collimator/detector has been designed for real-time dosimetry as well as B-10 concentration distribution map in the phantom that placed in front of the therapeutic neutron beam using the Monte Carlo simulation code MCNP6. Maximum Likelihood Expectation Maximization (MLEM) method has been used for image reconstruction which results 1 cm spatial resolution.

KEYWORDS

BNCT
SPECT
Boron distribution map
Tehran Research Reactor (TRR)
MLEM

HISTORY

Received: 3 December 2021
Revised: 20 December 2021
Accepted: 24 December 2021
Published: Winter 2022

1 Introduction

Boron Neutron capture Therapy (BNCT) is one of the promising methods for treating malignant tumors such as Glioblastoma Multiforme (a deep-seated tumor), Melanoma, neck and head tumors (superficial tumors) which cannot be treated with other treatments such as surgery (Wang et al., 2018; Barth et al., 1992, 2012; Miyatake et al., 2016; Barth et al., 2005; Yamamoto et al., 2008; Barth et al., 1999; Chadha et al., 1998; Kageji et al., 2011; van Rij et al., 2005a,b; Menéndez et al., 2009; Kato et al., 2004; Fukuda et al., 2003; Aihara and Morita, 2012). In this treatment method, a suitable B-10-contained drug with a high thermal neutron absorption cross-section, such as BPA (Menéndez et al., 2009), is injected into the body. The advantage of the BNCT treatment is a very large thermal neutron absorption cross-section in B-10 (∼3837 b), according to Eq. (1) (IAEA, 2001):

$$\begin{aligned} {}^{10}B + n \rightarrow \alpha + {}^{7}Li + 2.79\ \text{MeV} \\ \rightarrow \alpha + {}^{7}Li^{*} + 2.31\ \text{MeV} + \gamma(478\ \text{keV}) \end{aligned} \quad (1)$$

where the probability of occurrence of the first and the second interactions are 6% and 94%, respectively. According to this equation, 478 keV gamma-ray is emitted with the probability of 94% in each neutron absorption interaction. Also, the produced heavy particles (alpha and lithium) with high Linear Energy Transfer (LET) deposit their energies in the range of cell dimension (∼10 μm) and eventually destroy cancer cells. About 80% of the delivered dose in the BNCT is duo to boron dose (Minsky et al., 2011; Valda et al., 2005). Therefore, the therapeutic effect and efficiency of BNCT depend on the deposited dose in the tumor due to B-10.

The changes in boron concentration due to inhomogeneity or/and leakage of boron compound from the tu-

*Corresponding author: frahmani@kntu.ac.ir

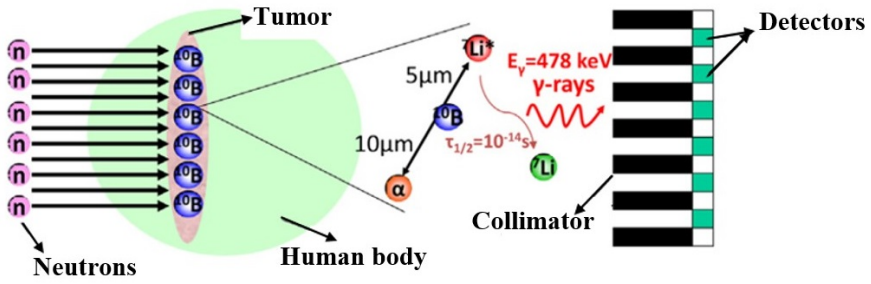

Figure 1: Principles of BNCT-SPECT method [24].

mor, affect the prescribed dose in the tumor and damage the normal surrounding tissues. Therefore, it is essential to have an accurate real-time monitoring of the boron concentration in irradiated organs (Minsky et al., 2011; Valda et al., 2005; Fatemi et al., 2018b; Verbakel and Stecher-Rasmussen, 1997; Kobayashi et al., 2000; Minsky et al., 2009; Murata et al., 2011; Manabe et al., 2016; Fatemi et al., 2018a,c; Gong et al., 2018).

There are several real-time and offline methods to determine the boron concentration with the aim of dosimetry in BNCT treatment (Paul and Lindstrom, 2000; Goorley et al., 2012; Molnar, 2004; Révay and Molnár, 2003; Egerton, 2011, 2008; Sodhi and Brion, 1984; Siegbahn, 2012; Bowman et al., 1973; Hadler et al., 1995; Montaser, 1998; Beauchemin, 2008; Taylor and Taylor, 2001; Bailey et al., 2005; Ollinger and Fessler, 1997; Muehllehner and Karp, 2006; Harris, 1986; Bovey et al., 1988; Lambert et al., 2019; Izewska and Rajan, 2005; Karsch et al., 2012; Ramani et al., 1997; Andrews et al., 1957; Venning et al., 2005; De Deene et al., 2000; Wagner and Hurst, 1958; Braby and Badhwar, 2001; Kliauga et al., 1989; Rikner and Grusell, 1987; Soubra et al., 1994). However, an accurate method for real-time calculation of the boron dose distribution map during irradiation is Single Photon Emission Computed Tomography (SPECT) (Minsky et al., 2011; Valda et al., 2005; Fatemi et al., 2018b; Verbakel and Stecher-Rasmussen, 1997; Kobayashi et al., 2000; Minsky et al., 2009; Murata et al., 2011; Manabe et al., 2016; Fatemi et al., 2018a,c; Gong et al., 2018), which uses gamma-rays to produce three-dimensional images of the body organs.

In general, the SPECT system consists of a gamma camera including the array of detectors and collimators for recording gamma-rays, as well as the software for image reconstruction using image processing methods. To achieve a three-dimensional image of B-10 distribution, the gamma camera must be rotated at different angles around the considered organ to record different projections from gamma-ray emissions (Minsky et al., 2011; Valda et al., 2005; Fatemi et al., 2018b; Verbakel and Stecher-Rasmussen, 1997; Kobayashi et al., 2000; Minsky et al., 2009; Murata et al., 2011; Manabe et al., 2016; Fatemi et al., 2018a,c; Gong et al., 2018). Finally, the image reconstruction algorithms are used to reconstruct the image of boron distribution (Rosenfeld et al., 2020; Bushberg et al., 2003). A schematic view of BNCT-SPECT as an accurate system with the aim of real-time dosimetry in BNCT is shown in Fig. 1.

Verbakel et al. (Verbakel and Stecher-Rasmussen, 1997) developed a gamma-ray telescope to detect the 478 keV prompt gamma-rays in the BNCT process. Kobayashi et al. (Kobayashi et al., 2000) combined the SPECT and Prompt Gamma Activation Analysis (PGAA) methods to design an ideal dose estimation system called PG-SPECT. Valda et al. (Valda et al., 2005) used a collimator and $LaCl_3$(Ce) detection array to develop an imaging system to measure the spatial distribution of the dose absorbed in the BNCT. Minsky et al. (Minsky et al., 2009) developed the SPECT system both experimentally and theoretically by using a collimator and the $LaBr_3$(Ce) detection array for real-time dosimetry in BNCT. Murata et al. (Murata et al., 2011) and Manabe et al. (Manabe et al., 2016) investigated the SPECT system by using a collimator and CdTe detection array. Fatemi et al. (Fatemi et al., 2018a,c) proposed a SPECT-based system by using CZT detectors for the BNCT process. Gang et al. (Gong et al., 2018) also studied the B-10 concentration in the tumor and reconstructed its image using a SPECT system.

In the present study, BNCT-SPECT, including collimator and detection arrays, has been designed for Tehran Research Reactor (TRR) using Monte Carlo simulation code MCNP6. TRR is the only possible neutron source for BNCT in Iran, as well as BNCT is an ongoing project for the Iranian research team, therefore the design of the BNCT-SPECT system has been studied for TRR using Monte Carlo simulation code MCNP6 (Goorley et al., 2012). Also, the Maximum Likelihood Expectation Maximization (MLEM) method has been used for the B-10 image reconstruction.

2 Materials and Methods

2.1 TRR and its therapeutic neutron beam

TRR is a 5 MW MTR (Material Test Reactor) pool-type research reactor. This reactor has 7 irradiation channels of different sizes and shapes as well as a thermal column containing graphite blocks (Kasesaz et al., 2014). The thermal column is composed of graphite and lead to obtain thermal neutrons for irradiation. It is possible to remove 9 graphite blocks in the first layer of the column. In addition, there is a space as large as a block in the central part of the second layer (Kasesaz et al., 2014). Therefore, a channel can be opened for neutrons and a suitable

treatment beam can be achieved.

In 2014, the designed Beam Shaping Assembly (BSA) based on the thermal column was proposed to achieve the optimum therapeutic neutron spectrum as illustrated in Fig. 2 (Kasesaz et al., 2014). This BSA includes aluminum (moderator), lead (reflector), bismuth (gamma-ray shield), and cadmium (thermal neutron filter).

2.2 Design of SPECT system for BNCT application

As stated before, SPECT system consists of detector and collimator arrays. Therefore, in this section, the design of the SPECT system including the collimator and detection array has been discussed.

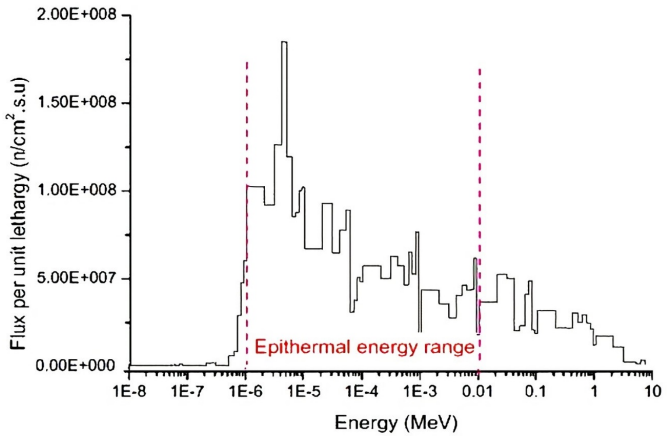

Figure 2: The TRR neutron beam spectrum at BSA port (Kasesaz et al., 2014).

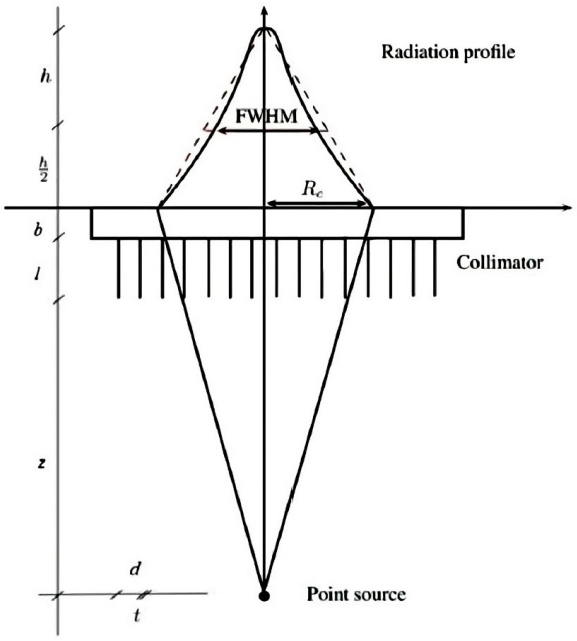

Figure 3: Schematic radiation profile of a gamma-ray point source placed in front of a parallel-hole collimator. (d= collimator's hole diameter, t= septum thickness) (Yazdandoust et al., 2021).

2.2.1 Collimator

The collimator is an important part of the imaging system for restricting the receiving angle to provide the spatial information of the detected radiation. The rays travelling parallel to the holes can cross the collimator and reach the detector, so the image of the source distribution can be constructed based on the responses of detectors. Since the geometric properties of the collimator considerably influence the image quality, it is necessary to choose the most appropriate one.

The collimator design has been carried out based on the following considerations: 1) the gamma-ray energy is specific (478 keV gamma-ray), so the beam attenuation in the collimator is measured according to this gamma-ray energy; 2) the distance between the gamma-ray source and the front face of the collimator is about 10 to 30 cm based on clinical applications (Wernick and Aarsvold, 2004).

Uncertainty of the origin of the detected photons for a point or linear source is modeled either by a Point Scattering Function (PSF) or a Linear Scattering Function (LSF), which is the radiation profile reflected by the collimator on the detector (Cherry et al., 2012). The Full Width at Half Maximum (FWHM) is considered as the spatial resolution of the collimator as shown in Fig. 3.

The spatial resolution is calculated according to Eq. (2) for a parallel-hole collimator:

$$R_c = \frac{d}{L_{\text{eff}}}(L_{\text{eff}} + b + z) \tag{2}$$

where, d is the diameter of the collimator hole, b is the distance between the rear face of the collimator and the middle part of the detector, and z is the vertical distance of the radiation source to the collimator. $L_{\text{eff}} = l - 2\mu^{-1}$ is the effective length of the collimator holes, where μ is the linear attenuation coefficient of the photons in the collimator material and l is the length of the holes or the thickness of the collimator (Cherry et al., 2012).

It should be noted that according to Eq. (2), for a certain diameter of the collimator hole, by increasing the distance between the source and the front face of the collimator, a longer hole is required to achieve the desired spatial resolution, which results in the reduced sensitivity of the collimator. Also, by increasing the distance of the source from the front face of the collimator in a certain length of the hole, a smaller diameter is needed to achieve better spatial resolution, which also reduces the sensitivity of the collimator. Therefore, according to the general clinical applications in nuclear medicine, and considering the feasibility of using the BNCT- SPECT, the distance between the source and the front face of the collimator has been selected as about 20 cm.

The collimator material must: 1) have a high attenuation coefficient for the gamma-ray to absorb scattered gamma-rays in the collimator material, and 2) produce fewer secondary photons for a high-quality image. Therefore, the collimator should be selected from materials with a high atomic number and density (Wernick and Aarsvold, 2004). The commonly-used collimator material is lead (Z = 82 and ρ =11.34 g.cm^{-3}), which is a better choice in comparison with gold or tungsten as far as the cost

and manufacturing complexities are concerned. Therefore, lead has been selected for the collimator design in this study. Also, a circular parallel hole collimator has been selected. Holes can be used in different shapes such as circles, triangles, squares, and hexagons, but based on the uniformity of exposure on the detectors, circular ones have been selected (Ziessman et al., 2013).

For determining the final arrangement of the collimator, different number of circular holes in collimator are compared in Fig. 4. As shown, based on 1) the maximum gamma-ray intensity in the central pixel in the detection array placed in the field of view of the tumor voxel and 2) by considering more reduction in gamma-ray count rate (low particle leakage) in the pixels around the central pixel in the detection array, a squared collimator with the single circular hole has been selected as the best choice.

Collimator array has been considered as large as the patient head (∼20 cm diameter) for an accurate mapping of full boron distribution map in GBM cases. Therefore, the optimal cross-section of the designed collimator has been considered a 20×20 cm^2.

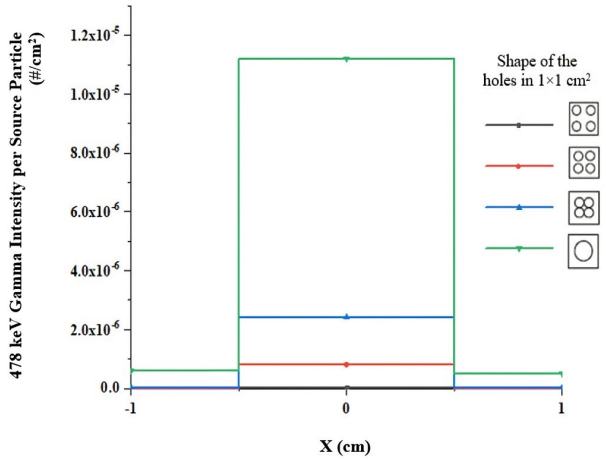

Figure 4: 478 keV gamma-ray intensity in the detection array pixels for different numbers of holes in each collimator. The gamma-ray source is on the axis of collimator at $x = 0$ cm.

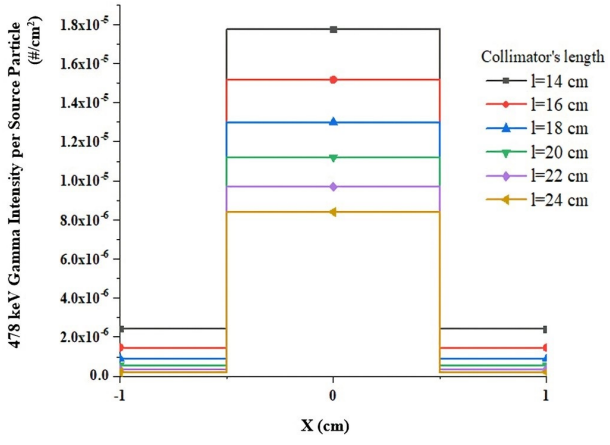

Figure 5: 478 keV gamma-ray intensity in the detection array pixels for different lengths of the collimator (*diameter* = 0.5 cm). The gamma-ray source is on the axis of collimator at $x = 0$ cm.

Spatial resolution and collimator sensitivity are two main factors in determining the quality of images in the SPECT, which are sufficient to ensure the correct operation of the imaging system (Wernick and Aarsvold, 2004).

As stated before, by increasing the length of the hole, as well as decreasing its diameter, the spatial resolution of the collimator is improved. However, the improvement in spatial resolution is accompanied by a decrease in the collimator sensitivity and the acceptance of fewer photons. Since, the collimators with better spatial resolution can provide a better image quality than the multipurpose collimator or more sensitive ones, the better spatial resolution is preferred to higher sensitivity. This means that there should be a tradeoff between sensitivity and spatial resolution of the collimator by selecting the optimal diameter and length of the holes.

Considering the requirements regarding the pixel dimension of the image, the spatial resolution of the collimator has been selected as 1 cm in this study. Therefore, the length and diameter of the holes should be determined according to the spatial resolution of Eq. (2), in which the desired spatial resolution of 1 cm is achieved by increasing the hole diameter. According to this, since the required length of the hole increases, the sensitivity is reduced, so the hole diameter has been set as 0.5 cm.

Another important factor to justify the accuracy of the selecting the length of hole is the gamma-ray intensity and count rate in the detection array pixels. As shown in Fig. 5, different collimator lengths have been simulated for 0.5 cm hole. To maximize the intensity of gamma-ray in the central pixel in the field of view of the source voxel, as well as a 95% reduction in 478 keV gamma-ray intensity in the pixels around the brightest pixel, a length of hole is selected 20 cm.

Septum, the wall between two adjacent holes, must be carefully selected to ensure minimum penetration from one hole to another. For a parallel-hole collimator, the septum is calculated according to Eq. (3):

$$\frac{t}{x} = \frac{2d + t}{\sqrt{l^2 + (2d + t)^2}} \tag{3}$$

where t is the thickness between the two adjacent holes in the collimator, d is the hole diameter, x is the length of lead that attenuates a given amount of 478 keV gamma-ray, and l is the length of the collimator hole, respectively (Valda et al., 2005).

Due to the energy-dependent attenuation coefficient of materials, the thickness of the septum is strongly dependent on the gamma-ray beam energy (Cherry et al., 2012). According to the gamma-ray energy of 478 keV and Eq. (3), as well as the 1 cm^3 voxel-size phantom, the selected diameter for the collimator hole, and with the aim of the corresponding effect of tumor voxels on the pixels in detection array with less penetration to surrounding pixels, the pixel has been also considered as 1 cm^2. In other words, the circular holes with 0.5 cm in diameter have been embedded in the center of 1 cm^2 square voxels (400 (20×20) detectors).

The collimator sensitivity is defined as the ratio of the number of gamma-rays passing through the collima-

tor holes to the number of gamma-rays emitted from the source, calculated according to Eq. (4) (Cherry et al., 2012):

$$g = K^2(\frac{d}{l_{\text{eff}}})^2\Big[\frac{d^2}{(d+t)^2}\Big] \quad (4)$$

This equation is obtained from collimator geometry and it depends on some factors such as septum (t), shape, diameter, and length of the holes. K is a constant coefficient that is a function of the shape and arrangement of the holes in the collimator. According to the selected septum, collimator's hole diameter, effective length of the collimator holes and 478 keV gamma intensity in the proposed detection array, K is calculated by simulation equal to 0.27. Therefore, the collimator sensitivity is 1.26×10^{-5} in this proposed design.

2.2.2 Detector

In this project, the CdZnTe detector has been selected, because semiconductor detectors such as CdTe and CdZnTe are superior in comparison with other detectors in various aspects such as energy resolution, detection efficiency, room temperature performance with a small cooling system, and small sizes (Bahnamiri, 2015; Kim et al., 2020).

To reach the maximum efficiency according to the collimator hole diameter (0.5 cm), the dimension of the entrance window of CdZnTe has been selected as 0.5×0.5 cm^2. Since one detector is positioned at the end of each hole, there is an array of 400 detectors corresponding to the array of collimators with 400 holes.

To select the appropriate thickness of CdZnTe, some important factors such as detection efficiency, leakage current and active detection volume of semiconductor detectors and cost-effectiveness should be taken into account. As shown in Fig. 6, the intrinsic efficiency of the CdZnTe with an entrance window of 0.5×0.5 cm^2 and the incident 478 keV gamma-rays for different detector thicknesses has been investigated.

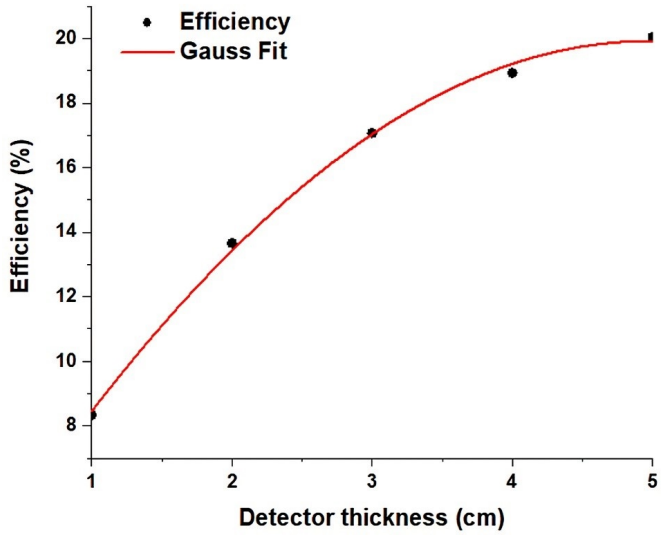

Figure 6: CdZnTe intrinsic efficiency with 0.5×0.5 cm^2 entrance window made in different thicknesses.

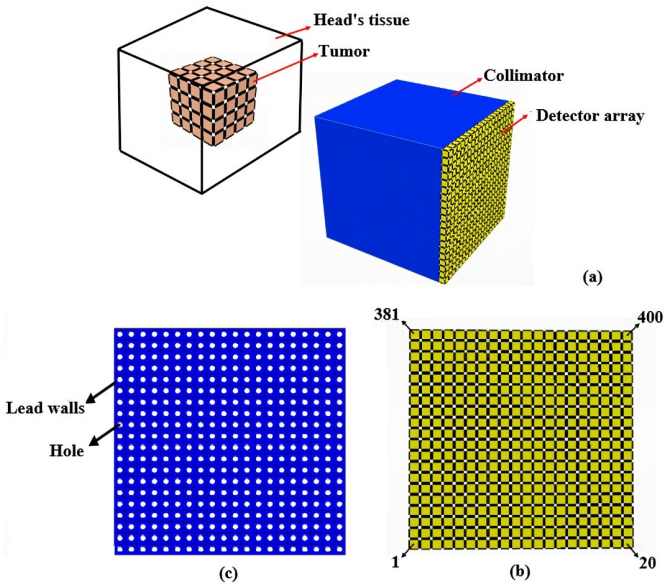

Figure 7: a) The schematic view of the proposed BNCT-SPECT system. b) The front view of the detection array (400 detectors). c) The front view of the collimator.

Considering a trade-off between the effective factors, the CdZnTe with a thickness of 2 cm has been selected. The 0.5×0.5×2 cm^3 CdZnTe detector made by IMEM is supposed to have the detection efficiency and energy resolution of about 6% and 3% at 478 keV, respectively (Fatemi et al., 2018b).

2.2.3 Phantom

To evaluate the accuracy, image quality, and performance of the designed SPECT system, a simple voxelized cubic phantom with the dimension of 4×4×4 cm^3 has been considered in the center of 20×20×20 cm^3 cubic phantom to simulate the tumor in the head, respectively. The dimension of the cubic phantoms has been selected as identical as possible to the actual dimensions of the tumor (∼2 cm in radius) and the human head (∼10 cm in radius). The schematic view of the designed SPECT system is shown in Fig. 7.

2.3 Image reconstruction of B-10 concentration distribution in tumor

To collect the required information to construct the SPECT image, the imaging system must rotate 360 degrees in predetermined angles around the organ of interest (Wernick and Aarsvold, 2004; Dahlbom and King, 2017). The smaller angle steps result in more data acquisition as well as a high-quality image, but at the expense of a longer imaging time. The tradeoff between the treatment time of about one hour and image quality (spatial resolution of 1 cm) leads to the angular step of about 9-degree, or equivalently, 40 angles around the phantom.

Since B-10 containing voxels in the BNCT method are those 478 keV gamma-ray emitters, each voxel has been considered as a volumetric source (voxel) of 478 keV gamma-ray. The image reconstruction can be performed

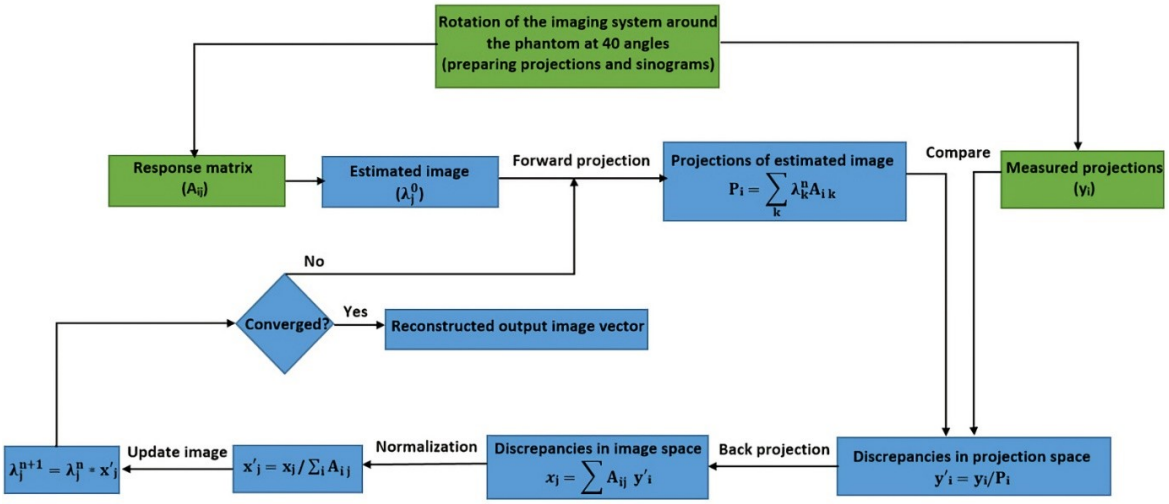

Figure 8: Flowchart of image reconstruction of B-10 concentration distribution in the tumor (green blocks: MCNP6, blue blocks: MATLAB).

by solving the equation $AB = C$; where C is the sinogram vector or the data obtained from the imaging, A is the response matrix and B is the B-10 distribution (the unknown vector). To create the response matrix, it is necessary to determine each detector response from each phantom voxel.

It has been supposed that the tumor phantom is made of cubic voxels for the calculations, therefore the gamma-ray intensity has been recorded on the detection array. For creating response matrix (A), each voxel has been boronated and the response of the detector array has been recorded in all 40 angles. Also, for the desired B-10 distribution, the response of the detector array in 40 angles has been recorded (C). Finally, the MLEM algorithm based on Eq. (5) has been used to obtain the unknown vector of the image reconstruction equation (B):

$$\lambda_j^{n+1} = \frac{\lambda_j^n}{\sum_i A_{ij}} \sum_i A_{ij} \left(\frac{y_i}{b_i + \sum_k \lambda_k^n A_{ik}} \right) \qquad (5)$$

where b_i is the background radiation, y_i is the count of energy peak related to i^{th} angles, A_{ij} is the image reconstruction matrix, and λ is also related to the MLE quantity for the j^{th} voxel in the n^{th} iteration (Wernick and Aarsvold, 2004; Dahlbom and King, 2017). For a 64-voxel tumor and the 40-angle rotations, together with a detection array of 400 pixels, matrix A will have 64 columns and 16000 (40×400) rows.

Due to the importance of achieving the arbitrary boron distribution effect in all detection array pixels and considering the presence of 400 detector pixels in the image reconstruction problem, the C vector has 16000 rows and one column. By substituting the response matrix and the sinogram vector in Eq. (5), the boron concentration distribution image (B) can be obtained. B has 64 rows and one column where each row indicates the probability of B-10 in each voxel of the tumor. The MLEM algorithm has been implemented using MATLAB software (Hanselman and Littlefield, 1996). The flowchart of the MCNP6 and MATLAB process to reconstruct the B-10 concentration distribution map in the tumor is shown in Fig. 8.

3 Results and discussion

To evaluate the accuracy and precision of the proposed SPECT system, with characteristics mentioned in Table 1, the MLEM technique for image reconstruction and the B-10 concentration distribution map has been discussed for two cases: 1) B-10 distribution in a single voxel and, 2) B-10 distribution in extensive voxels in the tumor. The tumor voxels are labeled according to Fig. 9.

3.1 B-10 distribution in a single voxel in the tumor

In this case, B-10 distribution is considered in only one specified voxel of the tumor. In other words, 478 keV gamma-rays have an isotropic emission just from one voxel. These voxels are located at different depths of the tumor. In these cases, gamma-ray emissions are sampled only from one voxel. For example, voxel No. 1 in the first layer of the tumor has been assumed as the 478 keV gamma source. The effect of this voxel on the detection array pixels for 10 angles (from 40 angles) is shown in Fig. 10 in which the tumor borders are marked with black lines.

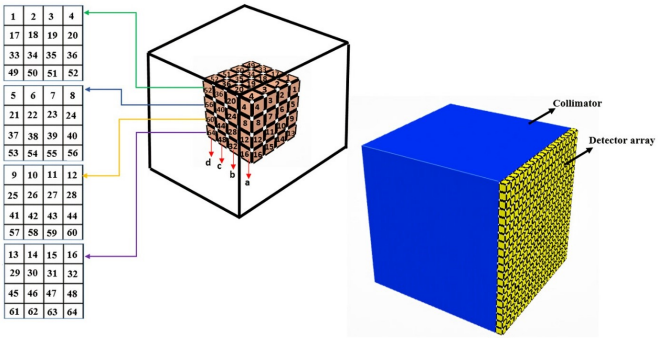

Figure 9: Numbering the tumor voxels. (a) to (d) depict the 1^{st}, 2^{nd}, 3^{rd}, and 4^{th} layer of the tumor.

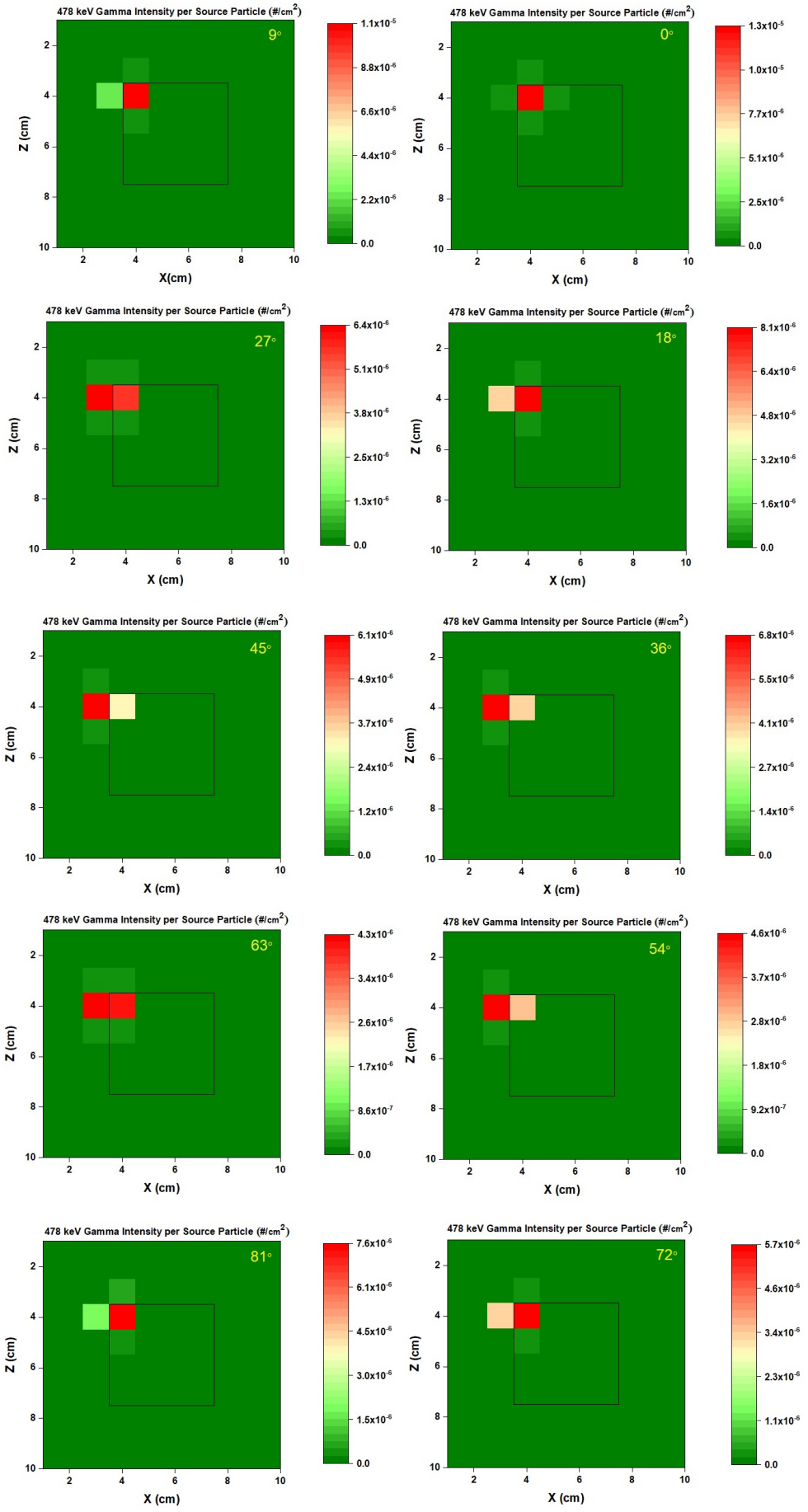

Figure 10: Response of the detection array to the distribution of B-10 in voxel No. 1 at 10 angles of the imaging system rotation.

Table 1: The basic characteristics of the proposed BNCT-SPECT system.

Parameter	Value
Material of collimator	Lead
Geometry of the collimator hole	Parallel circular hole
Length of collimator hole	20 cm
Diameter of collimator hole	0.5 cm
Septum	0.5 cm
General dimension of the collimator	$20\times20\times20$ cm^3
Spatial resolution of the collimator	1 cm
Sensitivity of collimator	1.26×10^{-5}
Type of detector	CdZnTe
Dimension of detector	$0.5\times0.5\times2$ cm^3
Efficiency of detector	6%
Energy resolution of the detector at 478 keV	3%

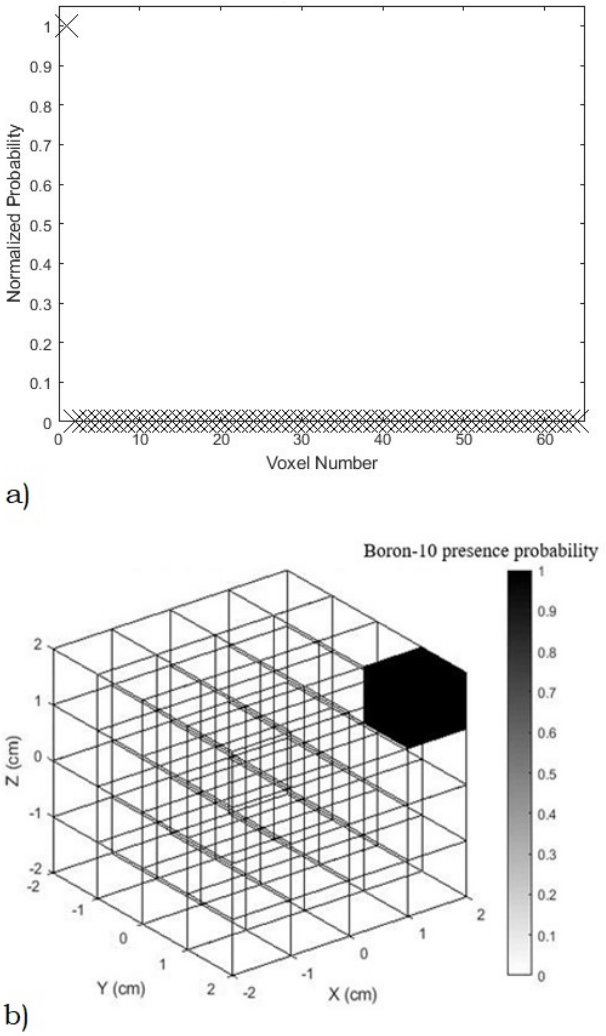

Figure 11: B-10 concentration image reconstructed for voxel No. 1 in the tumor using the MLEM method: a) 2-D, b) 3-D.

By applying the MLEM iterative image reconstruction method and repeating this algorithm several times, the B-10 distribution map in the tumor as the probability of B-10 presence in tumor voxel is obtained, as shown in Fig. 11. Also, the exact location of the B-10 distribution has been correctly identified in the tumor, as well as voxel No. 1 has the highest probability of B-10 presence (probability=1) and the reported probability for other voxels are zero. This means that voxel No. 1 is the 478 keV gamma-ray emitter and there is no B-10 in other voxels. In this study, an acceptable image of the B-10 distribution map can be obtained in the tumor with 100 repetitions.

3.2 B-10 distribution in extensive voxels in the tumor

In this case, several tumor voxels in different arrangements have been considered as 478 keV gamma-ray emitters sources simultaneously. A $3\times3\times3$ cm^3 boronated voxels in the tumor phantom (voxels No. 2, 3, 4, 6, 7, 8, 10, 11, 12, 18, 19, 20, 22, 23, 24, 26, 27, 28, 34, 35, 36, 38, 39, 40, 42, 43, 44) have been considered as 478 keV gamma-ray emitter source. The effect of the mentioned distribution on the detection array pixels in 10 angles (from 40 angles) around the tumor can be seen in Fig. 12. According to the results, the exact location of the 478 keV gamma-ray emission has been correctly identified as shown in Fig. 13.

The maximum probability of B-10 presence (probability=1) is related to the voxels considered as gamma-ray sources in the mentioned distribution. The probability of B-10 presence in other tumor voxels has been reported to be zero which indicates the B-10 absence in these voxels. As stated before, a 20 cm thick collimator has been considered in this study, so the variance reduction technique (dividing length of collimator into four parts and increasing the importance of the particles along the collimator's array using Geometry Splitting and Russian roulette) has been implemented for the collimator's geometry to achieve the results with low relative errors in a reasonable time. All MCNP6 input files have been run for 15 billion particles to obtain relative errors less than 3% with an average running time of about 10 hours in parallel processing. To create the response matrix, considering 40 angles around the tumor and considering 64 tumor voxels, 2560 (40×64) runs have been carried out. Due to the location of the voxels in the tumor and the symmetry in the detection array pixels, as well as in the angles of rotation, the number of codes has been reduced to 148. According to the calculation of 478 keV gamma-ray intensity in the detection array pixels (F4 Tally), these values can be converted to the number of gamma-rays by considering the correction coefficients such as TRR neutron source flux (0.65×10^9 n.cm^2.s^{-1}), ^{10}B$(n,\alpha)^7$Li reaction rate in the tumor (2.88×10^{-5} #.s^{-1}), the BNCT treatment time ($\sim$1 hour), and the detection efficiency (6 %).

The calculation error of gamma-ray intensity in each pixel of detection array in the field of view of the source voxels is less than 3%. Considering the Minimum Detectable Activity (MDA), the gamma-ray intensities in the pixels around the brightest pixel in the field of view of the source voxel are significantly lower than MDA, also it never contributes in the count of the detection array pixels, so they can be considered as zero or noise. According to the calculations of the background gamma radiation, the gamma counts less than 4 in the detector with 95% in confidence level has been considered as the noise.

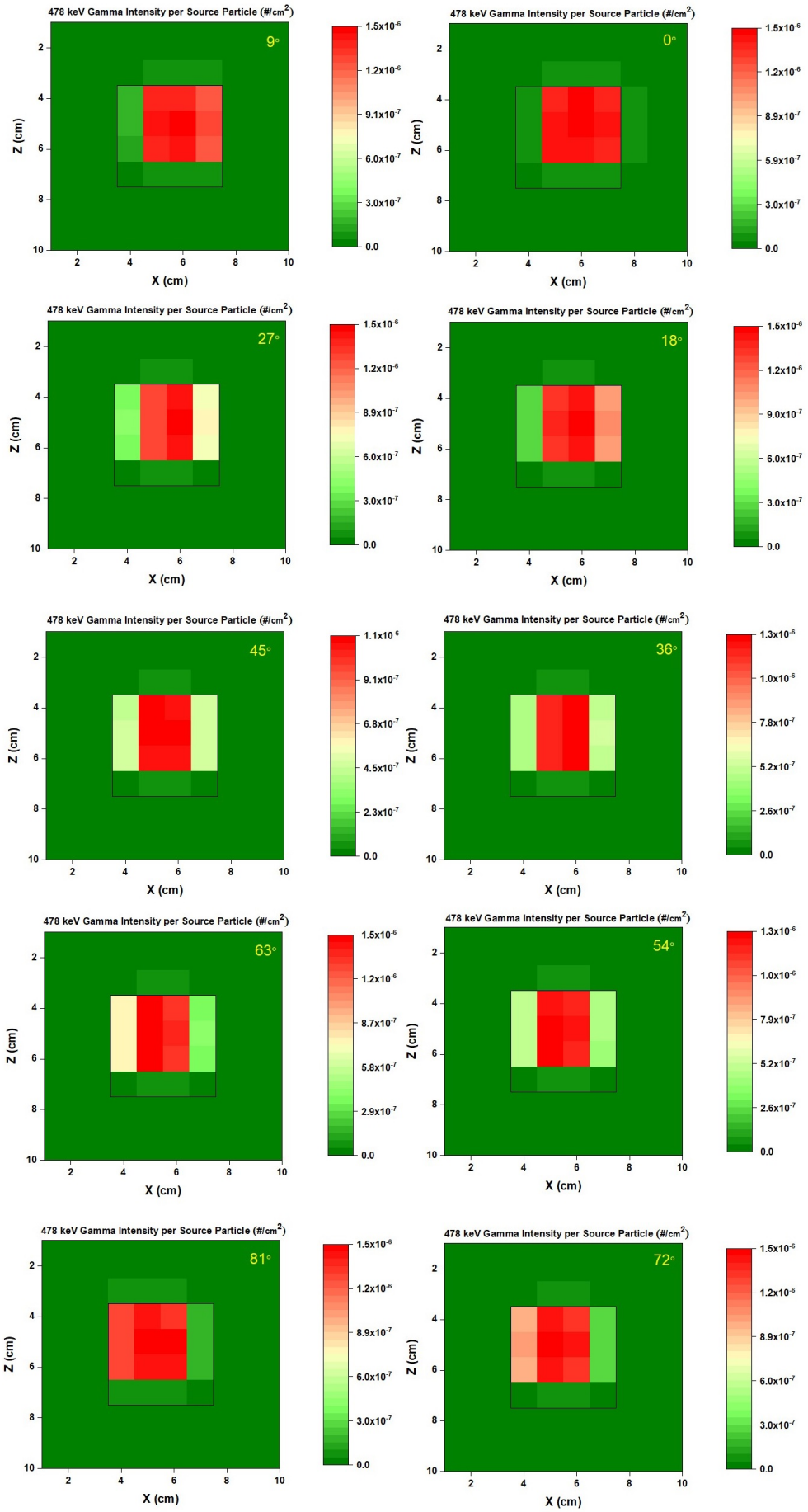

Figure 12: Response of the detector array for a borated tumor phantom (64-voxel) with a dimension of 3×3×3 cm^3 at 10 angles of the imaging system rotation.

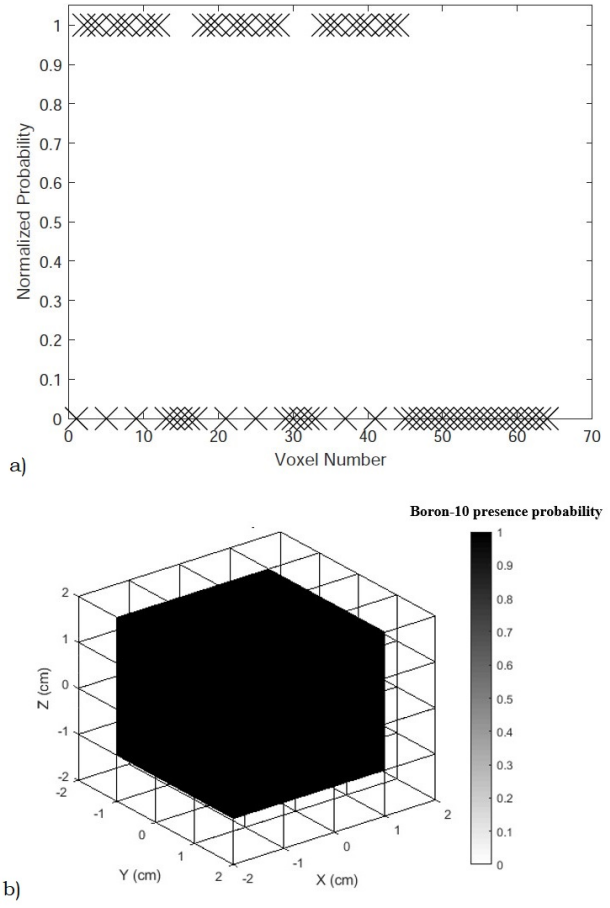

Figure 13: B-10 concentration image reconstruction for a borated tumor phantom (64-voxel) with dimension of 3×3×3 cm^3 using the MLEM method. a) 2-D, b) 3-D.

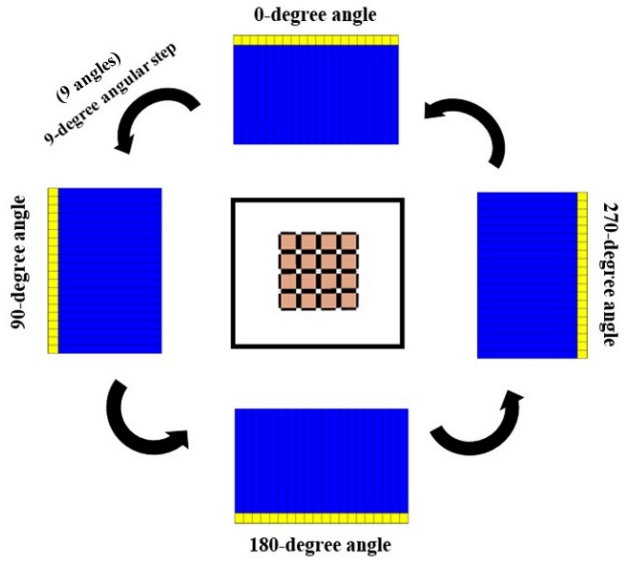

Figure 14: The proposed arrangement of the SPECT system around the phantom for imaging.

As mentioned before, background radiation has been ignored in this study, therefore the 478 keV gamma-ray count recorded in the pixels of detection array is the net count caused by the $^{10}B(n,\alpha)^7Li$ interaction. Number of gamma-rays recorded in a single pixel of the detector array located in the field of view of the tumor voxel can be determined using the correction coefficients. For example, one 478 keV gamma-ray at the zero-degree angle has been recorded in the detection array pixels.

One possible way to increase the number of gamma-rays in the pixels of detection array is to increase the counting time in each angle, which is 1.5 min for each angle with one-array SPECT and 40 angles of rotation. But in accordance with the limitation in the treatment time (less than one hour), the effectual idea is the increase in the number of the imaging array, for example 4 arrays around the phantom head to the counting time to 6 min. Another inappropriate solution may be the larger angular steps that result in less quality in the image. Therefore, as shown in Fig. 14, simultaneous 4-array SPECT around the phantom is recommended to collect the information needed to reconstruct the B-10 concentration distribution image in the tumor to increase the gamma-ray counts in the detection array pixels. The proposed system in this study can be also used in systems with higher therapeutic neutron flux, because the TRR epithermal neutron flux cannot be increased and it is a bit far from the IAEA recommendation for treatment.

4 Conclusion

Considering the necessity of real-time measurement of B-10 concentration as well as B-10 dose distribution during BNCT treatment, the 4-array BNCT-SPECT system based on TRR is proposed for real-time dosimetry for the first time in Iran. Also, the reconstructed image using the MLEM reconstruction method results in a 1 cm spatial resolution. Spatial resolution better than 1 cm can be achieved by arrays with more collimators and detectors. Also, the background radiation in the measurement field is being considered for the future development works.

References

Aihara, T. and Morita, N. (2012). Bnct for advanced or recurrent head and neck cancer. In *Neutron Capture Therapy*, pages 417–424. Springer.

Andrews, H. L., Murphy, R. E., and LeBrun, E. J. (1957). Gel dosimeter for depth-dose measurements. *Review of Scientific Instruments*, 28(5):329–332.

Bahnamiri, S. B. (2015). Investigation of collimator influential parameter on SPECT image quality: a Monte Carlo study. *Journal of Biomedical Physics & Engineering*, 5(1):39.

Bailey, D. L., Maisey, M. N., Townsend, D. W., et al. (2005). *Positron emission tomography*, volume 2. Springer.

Barth, R. F., Coderre, J. A., Vicente, M. G. H., et al. (2005). Boron neutron capture therapy of cancer: current status and future prospects. *Clinical Cancer Research*, 11(11):3987–4002.

Barth, R. F., Soloway, A. H., Fairchild, R. G., et al. (1992). Boron neutron capture therapy for cancer, realities and prospects. *Cancer*, 70(12):2995–3007.

Barth, R. F., Soloway, A. H., Goodman, J. H., et al. (1999). Boron neutron capture therapy of brain tumors: an emerging therapeutic modality. *Neurosurgery*, 44(3):433–450.

Barth, R. F., Vicente, M. H., Harling, O. K., et al. (2012). Current status of boron neutron capture therapy of high grade gliomas and recurrent head and neck cancer. *Radiation Oncology*, 7(1):1–21.

Beauchemin, D. (2008). Inductively coupled plasma mass spectrometry. *Analytical Chemistry*, 80(12):4455–4486.

Bovey, F. A., Mirau, P. A., and Gutowsky, H. (1988). *Nuclear magnetic resonance spectroscopy*. Elsevier.

Bowman, J., Hyde, E., and Eppley, R. (1973). Alpha spectroscopy of isotopes produced by high-energy nuclear reactions. *LBL-1666*, page 4.

Braby, L. and Badhwar, G. (2001). Proportional counter as neutron detector. *Radiation measurements*, 33(3):265–267.

Bushberg, J. T., Seibert, J. A., Leidholdt Jr, E. M., et al. (2003). The essential physics of medical imaging.

Chadha, M., Capala, J., Coderre, J. A., et al. (1998). Boron neutron-capture therapy (BNCT) for glioblastoma multiforme (GBM) using the epithermal neutron beam at the Brookhaven National Laboratory. *International Journal of Radiation Oncology* Biology* Physics*, 40(4):829–834.

Cherry, S. R., Sorenson, J. A., and Phelps, M. E. (2012). *Physics in nuclear medicine e-Book*. Elsevier Health Sciences.

Dahlbom, M. and King, M. A. (2017). Principles of SPECT and PET imaging. In *Physics of PET and SPECT Imaging*, pages 25–62. CRC Press.

De Deene, Y., Hanselaer, P., De Wagter, C., et al. (2000). An investigation of the chemical stability of a monomer/polymer gel dosimeter. *Physics in Medicine & Biology*, 45(4):859.

Egerton, R. F. (2008). Electron energy-loss spectroscopy in the TEM. *Reports on Progress in Physics*, 72(1):016502.

Egerton, R. F. (2011). *Electron energy-loss spectroscopy in the electron microscope*. Springer Science & Business Media.

Fatemi, S., Abbene, L., Principato, F., et al. (2018a). High performance 3D CZT spectro-imager for BNCT-SPECT: preliminary characterization. In *2018 IEEE Nuclear Science Symposium and Medical Imaging Conference Proceedings (NSS/MIC)*, pages 1–3. IEEE.

Fatemi, S., Altieri, S., Bortolussi, S., et al. (2018b). Preliminary characterization of a CdZnTe photon detector for BNCT-SPECT. *Nuclear Instruments and Methods in Physics Research Section A: Accelerators, Spectrometers, Detectors and Associated Equipment*, 903:134–139.

Fatemi, S., Bortolussi, S., Magni, C., et al. (2018c). Prompt gamma tomography for BNCT-SPECT: a feasibility study using small animal phantoms. In *2018 IEEE Nuclear Science Symposium and Medical Imaging Conference Proceedings (NSS/MIC)*, pages 1–5. IEEE.

Fukuda, H., Hiratsuka, J., Kobayashi, T., et al. (2003). Boron neutron capture therapy (BNCT) for malignant melanoma with special reference to absorbed doses to the normal skin and tumor. *Australasian Physics & Engineering Sciences in Medicine*, 26(3):97.

Gong, C., Tang, X., Fatemi, S., et al. (2018). A Monte Carlo study of SPECT in boron neutron capture therapy for a heterogeneous human phantom. *International Journal of Radiation Research*, 16(1).

Goorley, T., James, M., Booth, T., et al. (2012). Initial MCNP6 release overview. *Nuclear Technology*, 180(3):298–315.

Hadler, J., Iunes, P., Paulo, S., et al. (1995). A discussion of the reliability of alpha-spectroscopy using CR-39 and an image processor. *Radiation Measurements*, 25(1-4):749–752.

Hanselman, D. and Littlefield, B. (1996). *Mastering MATLAB: a comprehensive tutorial and reference*. Prentice-Hall, Inc.

Harris, R. K. (1986). Nuclear magnetic resonance spectroscopy.

IAEA (2001). Current status of neutron capture therapy. *IAEA-TECDOC-1223*.

Izewska, J. and Rajan, G. (2005). Radiation dosimeters. *Radiation oncology physics: A Handbook for teachers and students*, pages 71–99.

Kageji, T., Mizobuchi, Y., Nagahiro, S., et al. (2011). Clinical results of boron neutron capture therapy (BNCT) for glioblastoma. *Applied Radiation and Isotopes*, 69(12):1823–1825.

Karsch, L., Beyreuther, E., Burris-Mog, T., et al. (2012). Dose rate dependence for different dosimeters and detectors: TLD, OSL, EBT films, and diamond detectors. *Medical Physics*, 39(5):2447–2455.

Kasesaz, Y., Khalafi, H., and Rahmani, F. (2014). Design of an epithermal neutron beam for BNCT in thermal column of tehran research reactor. *Annals of Nuclear Energy*, 68:234–238.

Kato, I., Ono, K., Sakurai, Y., et al. (2004). Effectiveness of BNCT for recurrent head and neck malignancies. *Applied Radiation and Isotopes*, 61(5):1069–1073.

Kim, M.-S., Shin, H.-B., Choi, M.-G., et al. (2020). Reference based simulation study of detector comparison for BNCT-SPECT imaging. *Nuclear Engineering and Technology*, 52(1):155–163.

Kliauga, P., Rossi, H., and Johnson, G. (1989). A multielement proportional counter for radiation protection measurements. *Health physics*, 57(4):631–636.

Kobayashi, T., Sakurai, Y., and Ishikawa, M. (2000). A noninvasive dose estimation system for clinical BNCT based on PG-SPECTConceptual study and fundamental experiments using HPGe and CdTe semiconductor detectors. *Medical physics*, 27(9):2124–2132.

Lambert, J. B., Mazzola, E. P., and Ridge, C. D. (2019). *Nuclear magnetic resonance spectroscopy: an introduction to principles, applications, and experimental methods*. John Wiley & Sons.

Manabe, M., Sato, F., and Murata, I. (2016). Basic detection property of an array-type cdte detector for BNCT–SPECT–Measurement and analysis of anti-coincidence events. *Applied Radiation and Isotopes*, 118:389–394.

Menéndez, P., Roth, B., Pereira, M., et al. (2009). Bnct for skin melanoma in extremities: updated argentine clinical results. *Applied Radiation and Isotopes*, 67(7-8):S50–S53.

Minsky, D. M., Valda, A., Kreiner, A., et al. (2009). Experimental feasibility studies on a SPECT tomograph for BNCT dosimetry. *Applied Radiation and Isotopes*, 67(7-8):S179–S182.

Minsky, D. M., Valda, A., Kreiner, A., et al. (2011). First tomographic image of neutron capture rate in a bnct facility. *Applied Radiation and Isotopes*, 69(12):1858–1861.

Miyatake, S.-I., Kawabata, S., Hiramatsu, R., et al. (2016). Boron neutron capture therapy for malignant brain tumors. *Neurologia Medico-Chirurgica*, pages ra–2015.

Molnar, G. (2004). *Handbook of prompt gamma activation analysis: with neutron beams*, volume 1. Springer Science & Business Media.

Montaser, A. (1998). *Inductively coupled plasma mass spectrometry*. John Wiley & Sons.

Muehllehner, G. and Karp, J. S. (2006). Positron emission tomography. *Physics in Medicine & Biology*, 51(13):R117.

Murata, I., Mukai, T., Nakamura, S., et al. (2011). Development of a thick CdTe detector for BNCT–SPECT. *Applied Radiation and Isotopes*, 69(12):1706–1709.

Ollinger, J. M. and Fessler, J. A. (1997). Positron-emission tomography. *IEEE Signal Processing Magazine*, 14(1):43–55.

Paul, R. and Lindstrom, R. (2000). Prompt gamma-ray activation analysis: fundamentals and applications. *Journal of Radioanalytical and Nuclear Chemistry*, 243(1):181–189.

Ramani, R., Russell, S., and O'Brien, P. (1997). Clinical dosimetry using MOSFETs. *International Journal of Radiation Oncology, Biology, Physics*, 37(4):959–964.

Révay, Z. and Molnár, G. (2003). Standardisation of the prompt gamma activation analysis method. *Radiochimica Acta*, 91(6):361–369.

Rikner, G. and Grusell, E. (1987). General specifications for silicon semiconductors for use in radiation dosimetry. *Physics in Medicine & Biology*, 32(9):1109.

Rosenfeld, A. B., Biasi, G., Petasecca, M., et al. (2020). Semiconductor dosimetry in modern external-beam radiation therapy. *Physics in Medicine & Biology*, 65(16):16TR01.

Siegbahn, K. (2012). *Alpha-, beta-and gamma-ray spectroscopy*. Elsevier.

Sodhi, R. N. and Brion, C. (1984). Reference energies for inner shell electron energy-loss spectroscopy. *Journal of Electron Spectroscopy and Related Phenomena*, 34(4):363–372.

Soubra, M., Cygler, J., and Mackay, G. (1994). Evaluation of a dual bias dual metal oxide-silicon semiconductor field effect transistor detector as radiation dosimeter. *Medical physics*, 21(4):567–572.

Taylor, H. E. and Taylor, H. M. (2001). *Inductively coupled plasma-mass spectrometry: practices and techniques*. Academic Press.

Valda, A., Minsky, D., Kreiner, A., et al. (2005). Development of a tomographic system for online dose measurements in BNCT (Boron Neutron Capture Therapy). *Brazilian Journal of Physics*, 35(3B):785–788.

van Rij, C. M., Wilhelm, A. J., Sauerwein, W. A., et al. (2005a). Boron neutron capture therapy for glioblastoma multiforme. *Pharmacy World and Science*, 27(2):92–95.

van Rij, C. M., Wilhelm, A. J., Sauerwein, W. A., et al. (2005b). Boron neutron capture therapy for glioblastoma multiforme. *Pharmacy World and Science*, 27(2):92–95.

Venning, A., Hill, B., Brindha, S., et al. (2005). Investigation of the PAGAT polymer gel dosimeter using magnetic resonance imaging. *Physics in Medicine & Biology*, 50(16):3875.

Verbakel, W. F. A. R. and Stecher-Rasmussen, F. (1997). A γ-ray telescope for on-line measurements of low boron concentrations in a head phantom for BNCT. *Nuclear Instruments and Methods in Physics Research Section A: Accelerators, Spectrometers, Detectors and Associated Equipment*, 394(1-2):163–172.

Wagner, E. and Hurst, G. (1958). Advances in the standard proportional counter method of fast neutron dosimetry. *Review of Scientific Instruments*, 29(2):153–158.

Wang, L.-W., Liu, Y.-W. H., Chou, F.-I., et al. (2018). Clinical trials for treating recurrent head and neck cancer with boron neutron capture therapy using the Tsing-Hua Open Pool Reactor. *Cancer Communications*, 38(1):1–7.

Wernick, M. N. and Aarsvold, J. N. (2004). *Emission tomography: the fundamentals of PET and SPECT*. Elsevier.

Yamamoto, T., Nakai, K., and Matsumura, A. (2008). Boron neutron capture therapy for glioblastoma. *Cancer Letters*, 262(2):143–152.

Yazdandoust, H., Ghal-Eh, N., and Firoozabadi, M. (2021). TENISThErmal Neutron Imaging System for use in BNCT. *Applied Radiation and Isotopes*, 176:109755.

Ziessman, H. A., O'Malley, J. P., and Thrall, J. H. (2013). *Nuclear medicine: The requisites E-book*. Elsevier Health Sciences.